ACS APPLIED ELECTRONIC MATERIALS

pubs.acs.org/acsaelm

Article

Bias Sweep-Induced Analog Memristor Behavior, Using a Cuprous Iodide Thin Film, for Neuromorphic Computing

Rajesh Deb, Samapika Mallik, Yamineekanta Mishra, Roshan Padhan, Satyaprakash Sahoo, Kazuya Terabe, Tohru Tsuruoka,* and Saumya R. Mohapatra*

Cite This: *ACS Appl. Electron. Mater.* 2025, 7, 4616−4627

Read Online

ACCESS | Metrics & More | Article Recommendations | Supporting Information

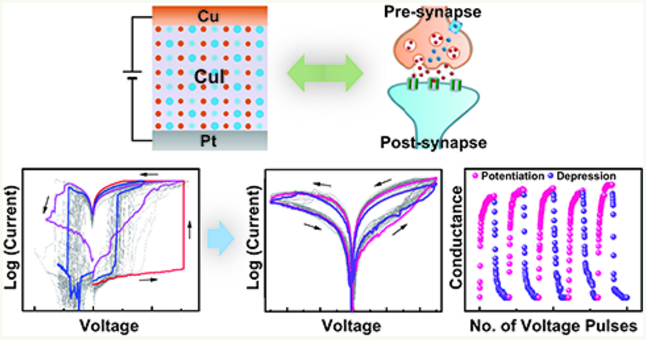

ABSTRACT: Mixed ionic-electronic conductors (MIECs) are known to show analog resistive switching (RS) behavior due to their coupled electronic and ionic transport properties. This study introduces a memristor device, made up of a well-known MIEC cuprous iodide (CuI), for artificial synaptic applications. A cross-point structured Cu/CuI/Pt device initially shows digital bipolar RS under bias voltage sweeping, which is characterized by well-separated SET and RESET voltages with a high ON/OFF resistance ratio of ∼10^5. After 100 bias sweeping cycles, the device completely changes, showing analog RS behavior without any well-defined SET and RESET voltage, and exhibits a continuous current trajectory under bias sweeps. In comparison to the digital RS mode, the analog RS mode exhibits minimal cycle-to-cycle variability with a reduced ON/OFF ratio of ∼10. The current conduction mechanism underlying the digital switching behavior is ascribed to the formation and dissolution of a Cu filament. The analog RS behavior arises from charge trapping/detrapping at defect sites created during digital RS cycles. The device showing analog RS exhibits long-term and short-term plasticity, similar to biological synapses under voltage pulse applications. Utilizing the long-term plasticity data, artificial neural network simulations demonstrate an image recognition accuracy of ∼93% for handwritten digits. Furthermore, the device successfully replicates paired-pulse facilitation/depression and spike timing-dependent plasticity. These findings indicate the great potential of the CuI-based analog memristor to serve as artificial synapses for neuromorphic computing applications.

KEYWORDS: *cuprous iodide, analog memristor, artificial synapse, mixed ionic-electronic conductor (MIEC), in-memory computing, artificial neural network (ANN)*

1. INTRODUCTION

As society becomes increasingly interconnected and with the prevalence of the Internet of Things and edge computing, the demand for faster and more energy-efficient computing systems is rapidly increasing. This need is further accelerated by the expansion of artificial intelligence technologies, which are transforming fields such as computer vision, gaming, language processing, and image classification.[1,2] However, the traditional computational paradigm, hindered by the limitations of Moore's Law and the von Neumann bottleneck, struggles to meet these escalating demands. To address these issues, non-Von Neumann architectures such as the in-memory computing (IMC) paradigm are gaining popularity. Inspired by the intricately parallel network structure of neurons and synapses in the human brain, which facilitates both computation and adaptive learning, IMC offers a promising avenue for overcoming the von Neumann memory bottleneck. In particular, IMC architectures, such as artificial neural network (ANN) accelerators, use vector-matrix multiplication (VMM) operations to mimic the weighted sum of inputs in a neural network layer. While traditional complementary metal-oxide-semiconductor (CMOS)-based technologies like graphic processing units and application-specific hardware accelerators have been developed to handle VMM operations, crossbar architectures using memristors are emerging as the most promising and energy-efficient solutions.[1,3]

Most of such memristors are made with oxide or dielectric films that exhibit digital (binary) memory states.[4,5] Although digital memory can be used for IMC applications, it needs to be greatly optimized in terms of pulsing parameters, circuit design, and modification of the ANN algorithm.[6,7] For example, in organic halide perovskite-based memristors showing typically digital switching, optimizations of pulse

Received: March 13, 2025
Revised: April 26, 2025
Accepted: May 6, 2025
Published: May 15, 2025

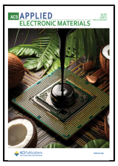

https://doi.org/10.1021/acsaelm.5c00529

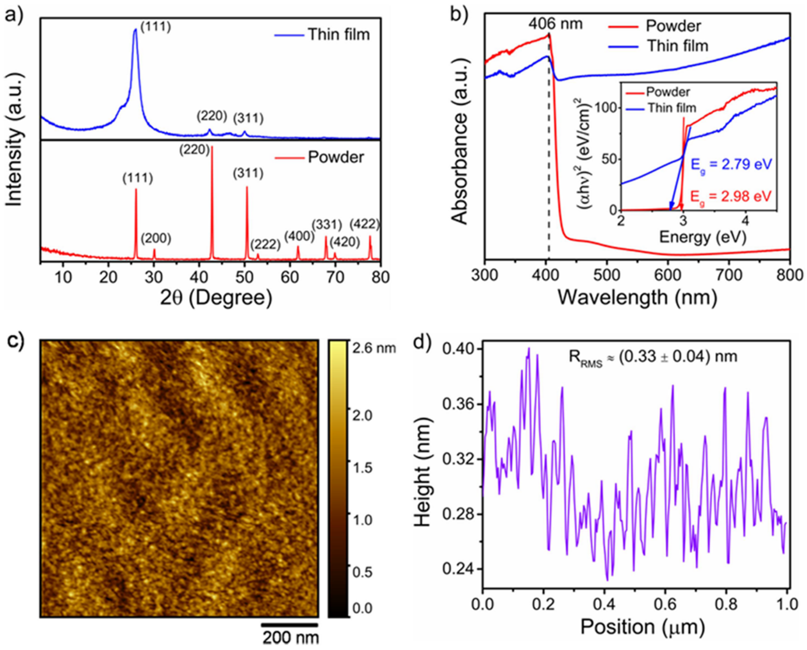

Figure 1. (a) XRD pattern and (b) UV−visible absorption spectra of CuI powder and a CuI thin film spin-coated on an SiO_2/Si substrate. The inset of (b) shows the Tauc plot used to determine the band gap energy of both CuI powder and thin film. (c) Typical AFM image of a CuI thin film coated on a SiO_2/Si substrate. (d) Typical cross-sectional line profile across the CuI film surface.

parameters are needed to find suitable analog memory windows for ANN operations.[7] From the material and memristor configuration point of view, lots of work has been reported on the conversion of digital memristors to analog memristors. This transition has been achieved utilizing various methods, such as introducing barrier layers, tuning the thickness of the switching layer, employing ligand exchange reactions, optimizing the electrodes, and so on.[8−11] In contrast to pure dielectrics/insulators, materials with conductivity linked to both ionic and electronic motions are favored for demonstrating analog memory capabilities.[12,13] Mixed ionic-electronic conductors (MIECs), endowed with superior electrical transport properties due to both ionic and electronic contributions, emerge as promising candidates for achieving analog-type memristive behavior.[14] Notable examples of such materials include perovskites, metal halides/sulfides, lithiated transition-metal dichalcogenide materials, and organic MIECs, which are suitable for analog switching.[15−18]

Of such MIEC materials, cuprous iodide (CuI) stands out for its properties as a superionic conductor and a hole-conducting semiconductor. In terms of electronic conductivity, CuI is a *p*-type semiconductor, due to the presence of intrinsic copper (Cu) vacancies (V_{Cu}) that act as acceptors. It further displays a high hole mobility of ∼ 40 $cm^2\ V^{-1}\ s^{-1}$ and a band gap of around 3.1 eV.[19] However, the zinc-blende phase of CuI, which is stable at room temperature, exhibits the lowest electrical conductivity of its various polymorphs, ranging from 10^{-4} to 10^{-5} S cm^{-1}.[20] In particular, when CuI is deposited as a thin film, it inherently has significant iodine vacancies (V_I). Such V_I acts as a hole trap and reduces the overall electrical conductivity.[21] Through defect engineering, such conductivity can be adjusted, opening avenues for exploring CuI in memristive applications. Despite this potential, CuI has not been explored significantly as a memristive material for IMC and neuromorphic applications.[22−24] A few studies have reported memristors with Ag or Al as one electrode and CuI as the switching layer, formed by physical vapor deposition or by iodination of the Cu layer.[22,23] A Cu/CuI/Pt memristor showing nonvolatile logic operations has also been fabricated.[24] However, these memristors exhibited only digital switching behavior, which limits their effectiveness for ANN applications.

In this work, we fabricated a cross-point Cu/CuI/Pt memristor device using a CuI film spin-coated from its precursor solution. Optimizing the coating parameters enabled the reduction of the CuI film thickness down to 60 nm without any surface defects. The device initially exhibited digital resistive switching (RS) behavior, which is attributed to the formation and dissolution of a Cu filament based on Cu-ion transport and electrochemical reactions. After more than 100 cycles of bias sweeping, the device transitioned to analog RS behavior. This analog switching is associated with the trapping/detrapping of carriers (holes) by defects induced during digital RS cycles. The device showing analog RS demonstrated key synaptic functionalities such as long-term and short-term plasticity, which are similar to the functionality found in biological synapses. Leveraging potentiation and depression data, ANN simulations achieved an image recognition accuracy of ∼93%.

2. EXPERIMENTAL SECTION

The Cu/CuI/Pt devices were fabricated on a Si substrate covered with 200 nm-thick SiO_2, as illustrated in Figure S1 of the Supporting Information (SI). The substrate was cleaned by ultrasonication with acetone and ethanol, each for 10 min, followed by plasma ashing treatment in an O_2 atmosphere for 1 min. First, the patterning of the bottom electrode was made using maskless photolithography. Subsequently, 5 nm-thick Ti and 35 nm-thick Pt were deposited by electron-beam (EB) evaporation, followed by a lift-off process with remover PG. Then, the switching matrix (CuI) film was prepared using a solution-based method. To create a 0.5 molar CuI precursor solution, CuI powder (purchased from Sigma-Aldrich) was dissolved in an organic solvent. The CuI solution was stirred for 24 h at 300

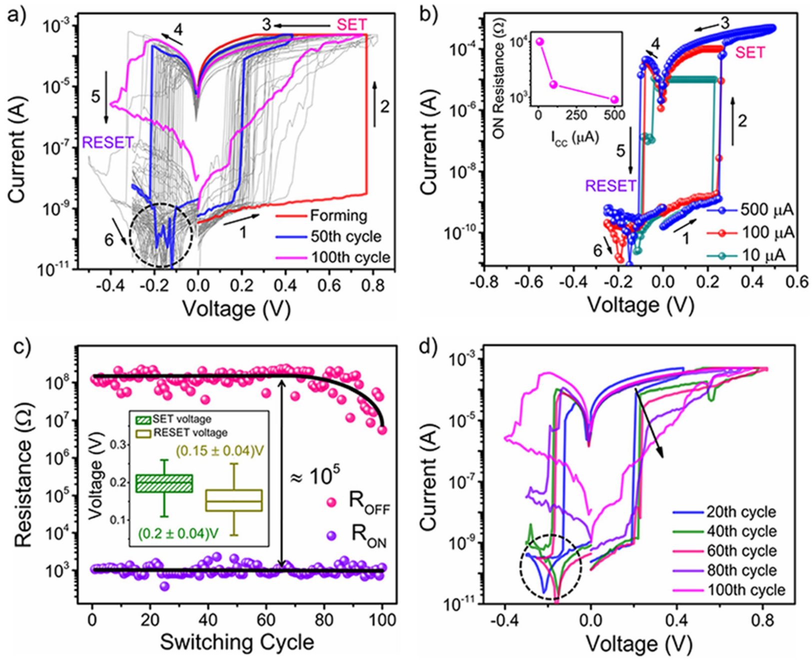

Figure 2. (a) Typical I−V characteristics of a Cu/CuI/Pt device showing digital bipolar RS behavior up to 100 sweep cycles. (b) I−V curves with different I_{CC}. The inset plots the ON resistances as a function of the I_{CC} value, read at 0.1 V after SET, showing multilevel ON states. (c) R_{ON} and R_{OFF} plots as functions of switching cycles. The inset displays the average SET and RESET voltages, with standard deviation. (d) Plot of I−V curves measured at every 20 cycles, illustrating the transition from digital to analog RS.

rpm to ensure homogeneity and then filtered through a filter paper. On the bottom Pt electrode, the CuI solution was spin-coated at 3000 rpm for 60 s with a slope time of 10 s. The coated film was annealed on a hot plate at 150 °C for 15 min to evaporate the solvent. It was found that the choice of solvents plays an important role in obtaining a homogeneous and pinhole-free CuI film. As shown in Figure S2 of SI, acetonitrile solution produced very nonuniform films. However, a mixture solution of 2-aminoethanol and 2-methoxyethanol at a 1:1 molar ratio produced a uniform and pinhole-free CuI film on a SiO_2/Si substrate.[24] The thickness of the resultant CuI film was measured as ∼60 nm using an optical thickness meter (Otsuka Denshi OPTM-F1). This film thickness was also confirmed by cross-sectional scanning electron microscopy, as shown in Figure S3 of the SI. Finally, 40 nm-thick Cu and 30 nm-thick Pt were EB deposited utilizing a shadow mask. This resulted in a cross-point structured Cu/CuI/Pt device with a junction area of 5 μm × 5 μm.

The structural properties of the CuI thin films spin-coated on SiO_2/Si substrates were analyzed using PANalytical Xpert[3] powder X-ray diffraction (XRD) with a Cu−Kα_1 source of wavelength 1.54 Å. The absorption spectra of the CuI film were examined by using an Agilent Cary 5000 UV−vis−NIR spectrophotometer. The surface topography of the CuI film was measured by atomic force microscopy (AFM) under ambient conditions using a Seiko Instruments Nano Navi E-sweep, with a Si cantilever in a noncontact mode. Electrical measurements of the fabricated devices, in both DC sweep and voltage pulse operations, were conducted at room temperature under ambient conditions by using a prober system equipped with a Keithley 4200 SCS/F semiconductor characterization system.

3. RESULTS AND DISCUSSION

3.1. Material Characterization. The XRD patterns of CuI powder and thin CuI film spin-coated on a SiO_2/Si substrate are shown in Figure 1a. The CuI powder is identified as being in the γ-phase, featuring a cubic zinc-blende structure.[25] Upon film formation from the solution, CuI remains in its γ-phase with predominant growth orientation along the (111) plane, accompanied by contributions from the (220) and (311) planes, exhibiting the polycrystalline nature of the coated CuI film. The preferred crystallographic orientation for the growth of thin CuI films along the (111) direction has been reported for various deposition techniques, including physical vapor deposition and solution-based methods.[26] This directional preference is attributed to the accelerated growth kinetics along that direction owing to the favorable stability energy dynamics at the growth interface. Moreover, the growth of CuI films along the (111) direction may increase the formation of V_I. This phenomenon can be explained primarily as being due to the difference in ionic radii between Cu and I species. The relatively small ionic radius of Cu (0.074 nm) with the comparatively larger ionic radius of I (0.206 nm) promotes the close-packed (111) lattice planes by pressing iodide, consequently increasing the likelihood of vacancy generation in the crystalline lattice.[27] The (111) Bragg peak of the CuI thin film was significantly broader than that of the CuI powder, as seen in Figure 1a. The average crystallite size along the (111) was reduced to ∼5.43 nm in the thin film, compared to 36.48 nm for the bulk powders as estimated using the Debye−Scherrer formula. The smaller crystallite size of CuI in the film has opposite effects on the transport properties of Cu ions and holes. The increase in volume fraction of the grain boundaries due to reduced crystallite size provides preferential paths for Cu ion transport.[24] On the other hand, the grain boundary scattering lowers hole mobility.[28,29]

The UV−visible absorption spectra of CuI powder and thin CuI film coated on an SiO_2/Si substrate are displayed in Figure 1b, for wavelengths ranging from 200 to 800 nm. The CuI powder exhibited no absorption above 440 nm, whereas a notable absorption was observed in the CuI film. Both the CuI powder and thin film showed a peak at ∼406 nm, representing a characteristic feature of CuI.[30] The optical band gap energy was determined through Tauc plot analysis, as shown in the inset of Figure 1b. The band gap energy was estimated to be ∼2.98 eV for CuI powder and ∼2.79 eV for the thin film,

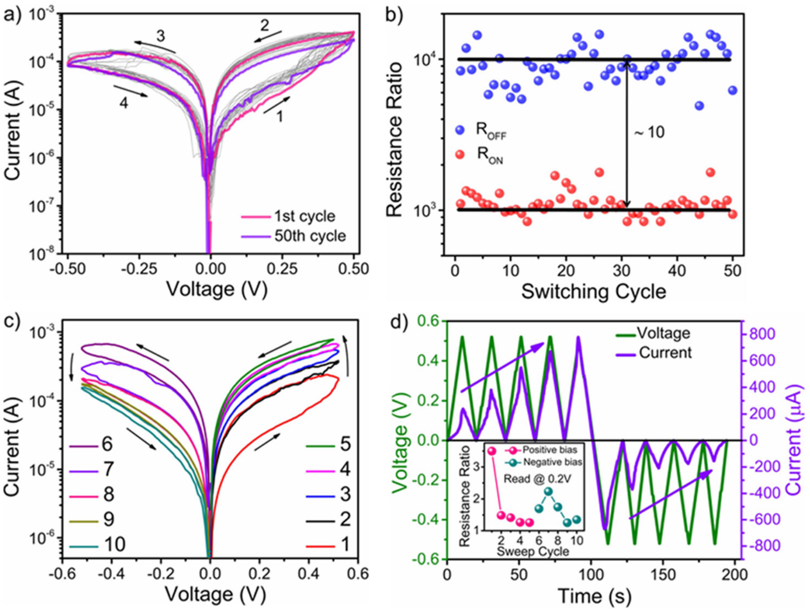

Figure 3. (a) Typical $I-V$ characteristics of a Cu/CuI/Pt device showing analog RS behavior for 50 sweep cycles. (b) ON and OFF resistances plotted as a function of switching cycles. (c) $I-V$ curves measured under five consecutive positive voltage sweeps (0 V → 0.5 V → 0 V) and the subsequent five consecutive negative voltage sweeps (0 V → −0.5 V → 0 V). (d) Temporal evolution of the current during five consecutive positive sweeps followed by five consecutive negative voltage sweeps. The inset depicts the memory window, defined by the ON/OFF resistance ratio, for consecutive gradual SET and RESET processes.

which aligns closely with reported values.[31] Note that the CuI film exhibits a higher absorbance due to the scattering of incident light by the film, which is due to granular structures with smaller grain sizes. Figure 1c presents an AFM image of a 60 nm-thick CuI thin film, measured over an area of 1 μm × 1 μm. The topography image revealed a smooth surface, representing uniform coverage of the CuI layer without any cracks or pinholes. The root-mean-square surface roughness (R_{RMS}) was evaluated to be ∼0.33 ± 0.04 nm, as shown in Figure 1d.

3.2. Electrical Characterization. The current–voltage ($I-V$) characteristics obtained from a Cu/CuI/Pt device are shown in Figure 2, which were measured under DC voltage sweeps. In all measurements, the Pt electrode was grounded, and a bias voltage was applied to the Cu electrode. The ON current was regulated by different current compliance values (I_{CC}) ranging from 10 to 500 μA, only for the positive bias sweep (the results of Figure 2a were obtained with an I_{CC} of 500 μA). The Cu/CuI/Pt device initially exhibited an OFF resistance (R_{OFF}) of greater than 10^8 Ω. When the bias voltage was swept in the positive direction, the current gradually increased and jumped to the compliance level of ∼0.8 V, as indicated by the red curve in Figure 2a. This corresponds to the first SET process from the OFF state to a low-resistance (ON) state, which is referred to as the forming process. As the bias voltage was subsequently swept to the negative direction, the device returned to the OFF state at ∼−0.3 V, corresponding to the RESET process. With increasing sweep cycles, the device exhibited digital RS behavior with lowered SET and RESET voltages, as indicated by the blue curve. The ON resistance (R_{ON}) can be tuned from 10^4 to less than 10^3 Ω by increasing the I_{CC} from 10 to 500 μA, as shown in Figure 2b, demonstrating multilevel ON states.

Figure 2c plots ON and OFF resistances as a function of switching cycles, which were taken from the measured $I-V$ curves of Figure 2a. It was found that both R_{ON} and R_{OFF} were stable up to ∼70 cycles with respective resistances of ∼10^3 and ∼10^8 Ω, resulting in an ON/OFF ratio of ∼10^5. The average SET and RESET voltages were estimated to be approximately 0.2 and −0.15 V, respectively, as shown in the inset of Figure 2c. As the switching cycle exceeded 70, the R_{OFF} gradually decreased, although the R_{ON} was unchanged, as indicated by the solid curves. The R_{OFF} dropped by nearly 2 orders of magnitude at the 100th cycle. This change in the RS behavior can also be observed in the $I-V$ curves. Figure 2d presents five $I-V$ curves, measured at every 20 cycles (from the 20th to the 100th cycle), which were extracted from Figure 2a. As the number of switching cycles increased (from the blue to purple curves), the current did not jump directly to the compliance value at the SET voltage but continued to increase even after the jump. The steepness of the current jumps gradually slowed, as indicated by the arrows. At the 100th cycle, the current no longer jumped and increased continuously, as indicated by the pink curve. A parameter to quantify such steepness is the turn-ON slope, which is known as the subthreshold slope in MOS field-effect transistors. The turn-ON slope is defined as the ratio of the voltage range to a decadal change in current, i.e., the inverse of the slope of the $I-V$ curve near the SET voltage.[32] It was calculated to be ∼ 4 mV/decade at the 20th cycle and significantly increased to ∼42 mV/decade at the 100th cycle. These results indicate that the device transitioned from digital RS mode to analog RS mode after 100 switching cycles. The same transition behavior was observed on different devices. The number of switching cycles required for the transition to analog RS varied slightly between devices, ranging from ∼60 to ∼100. Note that the current minima were always observed on the negative bias side, as indicated by the dashed circles in Figure 2a,d. The origin of these current minima will be discussed later.

Once the switching behavior has changed into analog RS mode, the device exhibited a stable, continuous switching behavior in a smaller bias voltage range. Figure 3a represents

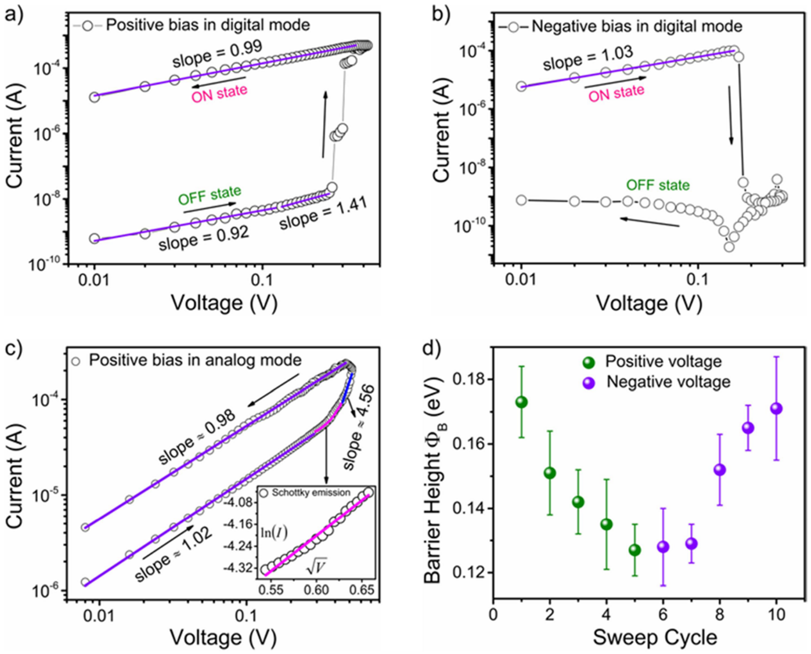

Figure 4. Log–log plots of I–V curves for the (a) SET process and (b) RESET process of the digital RS mode in a Cu/CuI/Pt device. (c) Log–log plot of an I–V curve for a positive voltage sweep of the analog RS mode. The inset represents an $ln(I)$ vs $\sqrt{V}$ plot with linear fitting in a voltage region between 0.28 and 0.43 V. (d) Variations of the Schottky barrier height (Φ_B) with consecutive positive and negative voltage sweeps in the analog RS mode.

the typical I–V characteristics of such analog RS behavior, measured between 0.5 and −0.5 V for 50 sweep cycles. As the voltage was swept on the positive bias side, the OFF state was gradually SET to the ON state. In the subsequent sweeping on the negative bias side, the ON state was again gradually RESET to the OFF state. The device exhibited highly stable analog RS behavior, with almost constant hysteresis, and significantly reduced cycle-to-cycle variations. Figure 3b plots the ON and OFF resistances as a function of the switching cycle, which were taken from the I–V curves of Figure 3a. The average ON and OFF resistances were 10^3 and 10^4 Ω, respectively, resulting in an ON/OFF resistance ratio of ∼10, which is significantly reduced by $\sim 10,^4$ compared to the digital RS behavior (Figure 2c). The turn-ON slope further increased to ∼152 mV/decade, indicating a smooth resistance change of the device in the measured voltage range.

Another illustration of the analog RS operation is presented in Figure 3c. In this measurement, the bias voltage was first swept on the positive voltage side with a sequence of 0 V → 0.5 V → 0 V for five consecutive cycles. The current increased gradually with increased sweep cycles, indicating a gradual decrease of the ON resistance, as shown by the I–V curves labeled 1–5. As the bias voltage was subsequently swept on the negative voltage side with a sweeping sequence of 0 V → −0.5 V → 0 V for five consecutive cycles, the current decreased gradually, as shown by the I–V curves labeled 6–10. The hysteresis of the current was always large for the first voltage sweep, becoming smaller and smaller with repeated sweeps, resulting in a decrease in resistance change. To get a clear picture of the change in device resistance with voltage sweeps, Figure 3c is replotted in Figure 3d as a temporal evolution of the current along with the bias voltage. The continuous application of consecutive positive and negative biases induced a gradual increase in the positive current peak, followed by a gradual decrease in the negative current peak. This continuous and gradual change of the device resistance upon bias applications is analogous to synaptic functions such as potentiation and depression of synaptic weight by an external stimulus. The inset shows that the memory window, defined by the ON/OFF resistance ratio, decreased with an increasing number of sweep cycles for positive and negative bias sweeps, respectively.

3.3. Switching Mechanisms for Digital and Analog Switching.

We investigated the switching mechanism of the Cu/CuI/Pt device in both digital and analog RS modes. First, we analyzed the I–V characteristics of the SET and RESET processes in the digital RS mode, as depicted in Figure 4a,b on a log–log scale, respectively. When the bias voltage is swept from 0 V to the positive direction, the device exhibits a linear relationship in the low voltage region from 0.01 to 0.12 V of the OFF state, fitted with a slope of 0.92 V, as shown in Figure 4a. As the bias voltage further increases to the high voltage region from 0.13 to 0.25 V, another linear behavior with a slope of 1.41 was observed. The current conduction mechanism for the whole voltage region (from 0 to 0.25 V) can be explained by the Mott–Gurney law for ion-hopping, which is expressed as[33]

$$I = 2zecav\exp\left(-\frac{w_a^0}{kT}\right)\sinh\left(\frac{azeE}{2kT}\right) \tag{1}$$

where z is the ionic charge, e is the electron charge, c is the concentration of mobile ions, a is the jump distance of ions, v is the frequency factor, w_a^0 is the energy barrier, k is the Boltzmann constant, T is the absolute temperature, and E is the applied electric field. Under a low electric field $\left(E \ll \frac{kT}{aze}\right)$ conditions, the current I is linearly dependent on E, similar to ohmic conduction, which is given by

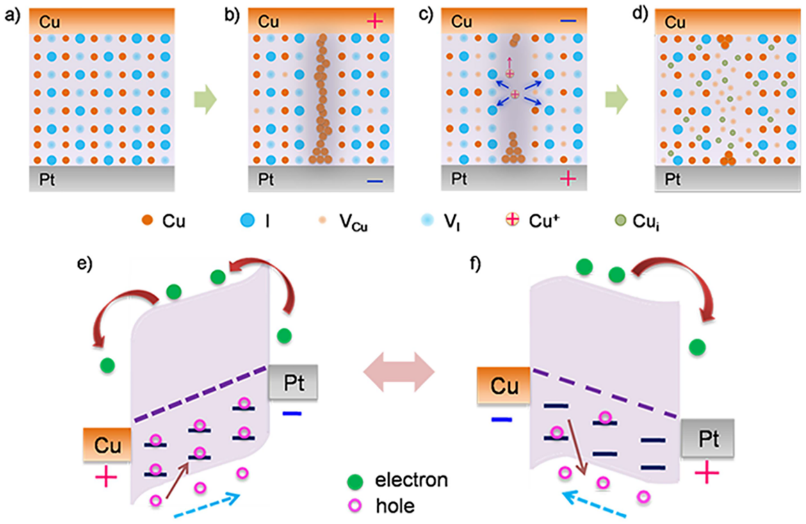

Figure 5. Switching mechanisms proposed for the digital and analog RS modes of a Cu/CuI/Pt device. (a) Pristine state of the device. (b) Formation and (c) dissolution of a Cu filament in the digital RS mode. (d) Device in the analog RS mode after digital RS cycles. Energy band diagrams of a Cu/CuI/Pt structure under (e) positive and (f) negative voltage bias to the Cu electrode in the analog RS mode.

$$I = \frac{(ze)^2 cE}{kT} a^2 v \exp\left(-\frac{w_a^0}{kT}\right) \tag{2}$$

For the high electric field ($E \gg \frac{kT}{aze}$), I varies exponentially with E, given by

$$I = zecav\exp\left(-\frac{w_a^0}{kT}\right)\exp\left(\frac{azeE}{2kT}\right) \tag{3}$$

The slopes of 0.92 and 1.41 observed for the low- and high-voltage regions coincide with the approximations of the Mott−Gurney law. Based on these fittings and the observed switching behavior, we attribute the observed digital RS switching to the formation and dissolution of a Cu filament between the two electrodes, due to the electrochemical metallization (ECM) mechanism.[34] Above a critical positive voltage, Cu is oxidized to Cu ions, and these ions migrate toward the Pt electrode through the CuI film. Then, a Cu filament is formed from the Pt electrode and bridged to the Cu electrode, resulting in the SET process. Therefore, the current jumps abruptly to the compliance level. After the SET process, the current slope of the ON state is ∼1 during the sweep back to 0 V, indicating Ohmic conduction of the Cu filament formed.[35] In the subsequent sweep to the negative direction, the current conduction is still governed by Ohmic conduction with a slope of ∼1, as shown in Figure 4b, indicating nonvolatile switching. Then, the RESET process takes place at a certain negative voltage (−0.17 V in Figure 4b), resulting in the dissolution of the Cu filament. The device returns to the OFF state with a current level of 1 nA.

To investigate the conduction mechanism of the analogue RS mode, the current in a positive voltage sweep of the analogue RS mode is plotted on a log−log scale, as displayed in Figure 4c. In the low voltage region from 0 to 0.28 V, the current exhibits a linear slope close to 1, indicating Ohmic conduction. However, the current increases nonlinearly in the intermediate voltage region from 0.28 to 0.42 V. This nonlinear segment is replotted as ln(I) vs sqrt(V) in the inset. The plot shows a well-fitted linear relationship, indicating that current conduction is governed by Schottky emission in this voltage region.[34] In the highest voltage region from 0.42 to 0.5 V, the current slope further increased to ∼4.56, suggesting that the current conduction is characterized by trap-assisted space-charge-limited conduction (SCLC).[36] After sweeping back from 0.5 V, the current slope again maintains a value close to 1 down to 0 V, suggesting Ohmic conduction in the ON state. In the subsequent negative bias sweep, the current follows the opposite sequence of Ohmic conduction, SCLC, Schottky emission, and again Ohmic conduction, as shown in Figure S4 of the SI. The charge carrier mobility μ can be calculated in the SCLC region by the Mott−Gurney law[34]:

$$\mu = \frac{8J_d d^3}{9\varepsilon\varepsilon_0 V^2} \tag{4}$$

where J_d is the current density, A is the junction area, d is the thickness of the CuI film, ε is the dielectric constant, ε_0 is the permittivity of vacuum, and V is the applied voltage. Considering the device structure, the charge carrier mobility was calculated to be ∼1.1 cm^2 V^{-1} s^{-1}, which agrees with the reported values.[20,37] The Schottky barrier height at the Cu/CuI interface was calculated from the I−V data of Figure 3c using the Richardson-Schottky equation, as presented in Figure 4d.[35] The result suggests that the barrier height decreases with successive positive voltage sweepings, while successive negative voltage sweepings increase the barrier height, which supports the continuous variation of the ON resistance. It was confirmed that the Schottky barrier height during the digital RS is much higher and the reduction of the barrier height under voltage sweeps is smaller than the analog RS, as shown in Figure S5 of the SI.

Another feature of the analog RS is the disappearance of the nanobattery effect, which is generally observed in ECM devices with an insulating switching layer.[38] Due to the ion concentration gradient, an electromotive force (emf) is inherently present during digital RS, as shown by the current minima in the dashed circles of Figure 2a,d. The current minimum observed after RESET processes corresponds to a nonzero-current crossing in a linear scale, as shown in Figure S6a and S6b of the SI. The emf was observed during digital RS mode but completely disappeared in the analog RS mode, as

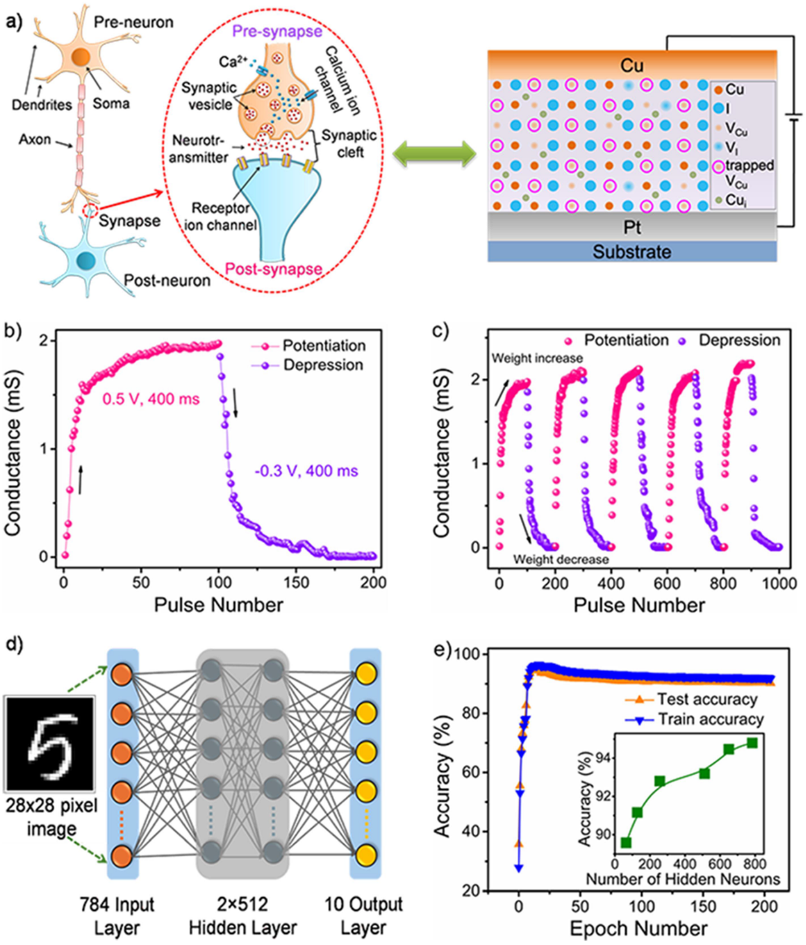

Figure 6. (a) Schematic showing the resemblance of the working mechanism of a biological synapse and a Cu/CuI/Pt analog RS device. (b) Typical LTP and LTD characteristics obtained with 100 consecutive positive pulses of 0.5 V and the subsequent 100 consecutive negative pulses of −0.3 V. (c) Endurance property of LTP/LTD characteristics for 5 cycles. (d) Schematic diagram of four-layer ANN with 784 input nodes, two 512 hidden nodes, and 10 output nodes for the classification of 28 × 28-pixel images from the MNIST data set. (e) Train and test accuracy plotted as a function of epoch numbers during neural network training. The inset shows the relationship between training accuracy and the number of hidden nodes.

seen in Figure 3a,c. The linear and enlarged plot of a representative analogue switching is shown in Figure S6c and S6d of the SI. These results suggest that the analogue RS mode is no longer based on the ECM mechanism and is associated with electronic contribution in a mixed conducting switching layer.

Based on the above considerations, we inferred the transition mechanism from digital and analog RS modes in the Cu/CuI/Pt device, as shown in Figure 5. The XRD result (Figure 1a) is suggestive of the presence of predominantly native donors, such as V_I, giving rise to a low hole concentration and reduced hole mobility. Therefore, the pristine Cu/CuI/Pt device exhibited a very high resistance of >1 GΩ (Figure 5a). The device initially exhibited digital RS behavior, which is attributed to the formation (Figure 5b) and dissolution (Figure 5c) of a Cu filament, based on the ECM mechanism. During these switching cycles, the concentration of Cu around the filament increases because a higher electric field promotes excess Cu ions to migrate toward the filament, giving rise to a Cu-rich environment. Density functional theory calculations revealed that V_{Cu} and Cu interstitials (Cu_i) have the lowest formation energies under Cu-rich conditions.[39] These defects act as shallow acceptors. Therefore, the significant decrease in R_{OFF} after 100 digital RS cycles can be attributed to the creation of Cu_i and V_{Cu} around the filament in the CuI film. The intrinsic V_I may be compensated by Cu antisites to form the neutral charge state,[40] which also contributes to the reduced OFF resistance.

After digital RS cycles, the insulating CuI matrix changed to the MIEC with higher electronic conductivity, as illustrated in Figure 5d. The subsequent analogue RS is explained using the band diagrams of the Cu/CuI/Pt device for both polarities, as illustrated in Figure 5e,f. The work functions of Cu, CuI, and Pt are 4.4, 5.05, and 5.6 eV, respectively.[34,37,41] In the equilibrium state, the Cu/CuI and CuI/Pt interfaces form Schottky and Ohmic contacts, respectively (the energy band diagrams before and after contact are illustrated in Figure S7 of the SI). When a positive bias voltage is applied to the Cu electrode, the Schottky barrier height at the Cu/CuI interface is reduced (Figure 5e), and the majority carriers (holes) become trapped in the shallow acceptor sites in the CuI film. Therefore, the device is turned ON. Conversely, when a negative bias voltage is applied, the Schottky barrier height at the Cu/CuI interface increases (Figure 5f), causing the charge carriers to be released from the acceptor sites, which turns the device OFF. This mechanism can also be corroborated by the

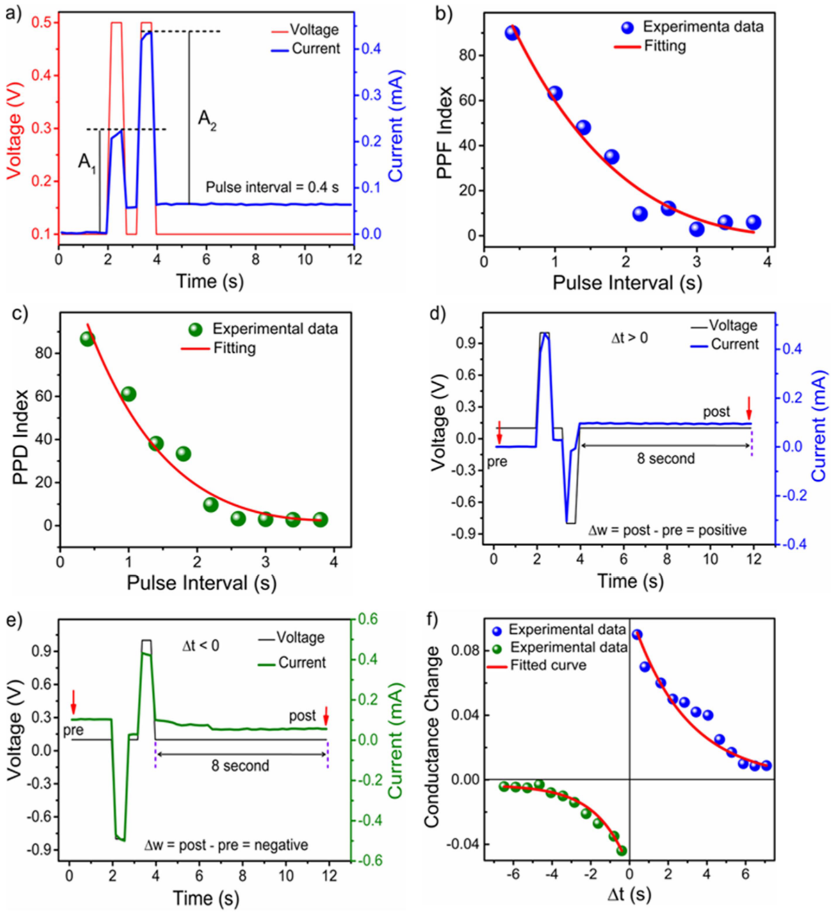

Figure 7. (a) Typical PPF behavior obtained from a Cu/CuI/Pt device under an application of two consecutive positive pulses with 0.5 V amplitude and 400 ms width. (b) PPF index plotted as a function of varied time intervals of the pulse pair. (c) PPD index plotted as a function of varied time intervals, obtained under an application of two consecutive negative pulses with −0.3 V amplitude and 400 ms width. A pre- and postsynaptic pulse pair applied to mimic Hebbian STDP for (d) $\Delta t > 0$ and (e) $\Delta t < 0$. (f) Conductance change plotted as a function of varied time intervals between pre- and postsynaptic pulses.

modulation of the Schottky barrier height during successive voltage sweeps, as shown in Figure 4d. The modulation of the barrier height with repetitive positive and negative biases is mainly determined by the trapping/detrapping of carriers in the CuI film, which in turn gives rise to analog RS behavior.

3.4. Long-Term and Short-Term Synaptic Plasticity. A biological synapse, comprising a presynaptic neuron and a postsynaptic neuron, is depicted in Figure 6a. The action potential arriving at the presynaptic membrane triggers the release of neurotransmitters at the synaptic cleft. These neurotransmitters bind to receptor ion channels on the postsynaptic membrane, inducing alteration in the membrane potential of the postsynaptic neuron.[42] This alteration is quantified as postsynaptic current. The analog RS behavior observed in our CuI-based device can be used to emulate synaptic functionalities, where Cu and Pt serve as analogous to the presynaptic and postsynaptic membranes, respectively. The synaptic processes crucial for long-term and short-term plasticity functions are realized through this emulation.[43] First, long-term potentiation (LTP) and depression (LTD) were investigated by the application of voltage pulses with different amplitudes, widths, and intervals. Figure 6b shows the LTP and LTD characteristics obtained with 100 consecutive positive pulses of 0.5 V and the subsequent 100 consecutive negative pulses of −0.3 V. The pulse width and interval time between pulses were fixed at 400 ms, respectively, and the device conductance was measured after each pulse with a read voltage of 0.1 V. The conductance increased (decreased) steeply for the initial 10 positive (negative) pulses and then increased (decreased) gradually with an increase in the number of positive (negative) pulses, which emulates the LTP and LTD functions of biological synapses, respectively. This LTP/LTD behavior is highly reproducible for 1,000 pulses (five LTP/LTD cycles), without any deterioration, as shown in Figure 6c, indicating good endurance behavior of the Cu/CuI/Pt device. The device also exhibited good retention properties of the ON state for at least up to 14 min after applying positive pulses, as shown in Figure S8 of the SI.

The nonlinearity of the observed LTP and LTD characteristics was evaluated by a widely used resistive memory-based synaptic model, given by the following equation:[44]

$$G = \begin{cases} ((G_{\mathrm{ON}}^{\alpha} - G_{\mathrm{OFF}}^{\alpha}) \times \omega + G_{\mathrm{OFF}}^{\alpha})^{1/\alpha} & \text{if \& } \alpha \neq 0 \\ G_{\mathrm{ON}}^{\alpha} \times (G_{\mathrm{ON}}/G_{\mathrm{OFF}})^{\omega} & \text{if \& } \alpha = 0 \end{cases} \quad (5)$$

where ω is the internal variable (ranging from 0 to 1), G_{ON} and G_{OFF} are the conductances of the ON and OFF states, respectively, and α represents the nonlinearity coefficient. From fitting of eq 5 to the LTP and LTD data with 20 voltage pulses, as shown in Figure S9 of the SI, the nonlinearity coefficients for LTP (α_{LTP}) and LTD (α_{LTD}) were evaluated to be 2.51 and 0.98, respectively. These parameters are essential in the off-chip training process for pattern classification with neural network training.[45] We performed ANN simulations using these nonlinear coefficients for supervised learning of handwritten digits from the Modified National Institute of Standards and Technology (MNIST) data set. Using the Pytorch package, training images were linearized to 784 × 1 input matrices with each pixel value normalized to [0, 1]. Then, the ANN network was constructed with 784 input nodes, two hidden layers with 512 nodes each, and 10 output nodes representing the digits "0" to "9", as shown in Figure 6d. The neural network training algorithm is based on the rectified linear unit (ReLU) activation function, which employs cross-entropy loss as the cost function. To achieve high recognition accuracy, the training process was repeated five times in each epoch. Figure 6e shows plots of the mean values of the training accuracy for 200 epoch cycles. It shows a peak accuracy of ~96%, which finally stabilized at ~93% after 50 epochs of the pattern recognition task during the training cycles. It was also confirmed that the test accuracy remains consistent with the training accuracy. The inset of Figure 6e delineates the stable accuracy values after 50 epochs, when the number of hidden neurons varied from 64 to 784. We found that the most stable accuracy is observed at 512 hidden nodes, although increasing the number of hidden neurons leads to a higher recognition rate. These results show the potential of CuI-based analog memristor arrays towards effective image recognition applications.

Paired pulse facilitation (PPF) and depression (PPD) represent distinct forms of short-term plasticity, entailing a temporary modulation of synaptic connection strength subsequent to two consecutive presynaptic action potentials. In particular, PPF elicits an augmentation in the postsynaptic current during the second action potential, but PPD induces a reduction in the same. In biological synapses, PPF is attributed to residual calcium accumulation within the presynaptic terminal, precipitating an increased release of synaptic vesicles and thereby amplifying neurotransmission. Conversely, PPD arises from vesicle depletion, leading to fewer neurotransmitters for release, hence attenuating synaptic transmission.[46] With our Cu/CuI/Pt device, the PPF behavior was achieved by applying a pair of identical positive pulses with an amplitude of 0.5 V and a pulse width of 400 ms. The current clearly increased due to the second pulse being greater than the first pulse, as shown in Figure 7a. The interval time between the pulse pair was varied from 400 ms to 3.84 s, and the PPF index was calculated using the formula $(A_2 - A_1)/A_1 \times 100\%$, where A_1 and A_2 represent the peak current values for the first and second voltage pulses, respectively. The PPF index exhibited a maximum value of ~90% at the shortest interval time (400 ms) and decreased to ~6% at 3.84 s, as shown in Figure 7b. The PPF index was analyzed using a double exponential function[47]:

$$\text{PPF index} = 100 + B_1 \exp\left(-\frac{\Delta t}{\tau_1}\right) + B_2 \exp\left(-\frac{\Delta t}{\tau_2}\right) \tag{6}$$

where Δt is the interval time between the first and second voltage pulses, B_1 and B_2 represent the amplitude of two exponential decay constants, and τ_1 and τ_2 are the relaxation time constants of the respective phases. From fitting eq 6 to the data of Figure 7b, c, τ_1 and τ_2 were found to be 2.38 and 8.34 s, respectively. For PPD behavior, a pair of identical negative pulses (−0.3 V, 400 ms) was applied with varied interval times. The current after the second spike became smaller than that after the first pulse, as shown in Figure S10 of the SI. The PPD index was calculated to be ~87% at $\Delta t = 400$ ms, and decayed exponentially to ~ 3% at $\Delta t = 3.84$ s, as shown in Figure 7c. The decay is well fitted with the double exponential function (eq 6), and τ_1 and τ_2 were estimated to be 1.4 and 15 s, respectively.

Spike-timing-dependent plasticity (STDP) is a form of long-term plasticity that constitutes a critical mechanism underlying learning and memory in biological synapses. In STDP, the synaptic weight is modulated by the order of appearance and the interval time (Δt) between pre- and postsynaptic action potentials. When the presynaptic spike arrives before the postsynaptic spike ($\Delta t > 0$), it results in an increase in connection strength between the two neurons, thereby inducing LTP. Conversely, if the presynaptic spike lags behind the postsynaptic spike ($\Delta t < 0$), it leads to the attenuation of connection strength, thereby inducing LTD.[48,49] The detailed input pulse scheme for STDP measurements is illustrated in Figure S11 of the SI. Figure 7d shows the typical result under an application of a pulse pair with $\Delta t > 0$, comprising a positive voltage pulse (1 V, 400 ms) as the presynaptic spike and a negative voltage pulse (−0.8 V, 400 ms) as the postsynaptic spike. Similarly, for $\Delta t < 0$, a pair of negative voltage pulses (−0.8 V, 400 ms) as the presynaptic spike and positive voltage pulse (1 V, 400 ms) as the postsynaptic spike were applied, as shown in Figure 7e.The resultant current was measured at 8 s after the postsynaptic spike. The change in synaptic weight was quantified as the difference between the conductances before and after the pulse pair. The gradual change of the conductance, depicting both LTP and LTD, is evident in the II and IV quadrants of Figure 7f, showcasing the dependency on the interval time of the pulse pair. The conductance change (ΔW) was fitted with the Hebbian STDP function, given by the following equations[47,49]:

$$\Delta W = \begin{cases} A_+ \exp\left(-\frac{\Delta t}{\tau_+}\right), & \Delta t > 0 \\ A_- \exp\left(-\frac{\Delta t}{\tau_-}\right), & \Delta t < 0 \end{cases} \tag{7}$$

where A_+, A_-, and τ_+, τ_- are the scale factors and decay time constants of the exponential functions, respectively. From fitting eq 7 to the data of Figure 7d, e, τ_+ and τ_- were estimated to be 2.86 and 1.65 s, respectively, which are values similar to the τ_1 obtained from the PPF and PPD behaviors. We see that the Hebbian scheme derived from fitting the STDP data follows an asymmetric Hebbian learning rule.[50] These results indicate that the Cu/CuI/Pt device can successfully emulate PPF/PPD and STDP behaviors, similar to what is exhibited by biological synapses.

The switching speed and energy consumption are crucial parameters for neuromorphic device applications that enable efficient and effective processing, closely mimicking the behavior of the human brain. In our measurements, the minimum pulse width that can induce the SET process is 100 ms. In order to switch the Cu/CuI/Pt device with a shorter pulse width, a higher voltage is required. However, we used voltage pulses with an amplitude of less than −0.7 V to limit the device operation to the analog RS mode. To observe the short-term and long-term plasticity, such as LTP/LTD, PPF/PPD, and STDP, voltage pulses with a 400 ms width were used. The energy consumption dE can be calculated using the following equation:[51]

$$dE = V \times I \times \Delta t \qquad (8)$$

where V is the amplitude of the input pulse, I is the maximum current to SET the device, and Δt is the pulse width. Using the experimental values V = 0.5 V, I = ∼0.95 mA, and Δt = 400 ms, the dE was estimated to be ∼190 μJ. We believe that the switching speed and energy consumption can be further improved by optimizing the material/device parameters and measurement conditions.

3.5. Comparison with Other CuI-Based Devices. Finally, we discuss the differences between our Cu/CuI/Pt analog memristor and other CuI-based RS devices. As mentioned in the Introduction, previous studies of CuI-based RS devices had primarily focused on their digital RS characteristics. Mishra et al. and Li et al. found digital RS with sharp SET and RESET processes in ITO/CuI/Ag and Pt/CuI/Cu devices, respectively.[22,24] CuI films were formed by the iodination of Cu and spin-coating of CuI precursor solutions using the same mixed solvents that we employed, resulting in 270 and 115 nm thick CuI films, respectively. They attributed the observed RS to the formation and dissolution of a Ag(Cu) filament. Assi et al. reported digital RS in a symmetric Al/CuI/Al device with a 100 nm thick CuI film deposited by thermal evaporation.[23] Their device exhibited digital RS with small SET and large RESET voltages in a wide voltage scan range of −3 to 3 V, and the observed switching was explained by charge trapping and detrapping. Bala et al. reported the RS of an ITO/CuI/Ag device with a CuI film spin-coated by CuI solution with acetonitrile.[52] Despite the thickness of the CuI film being only 20 nm, they claimed that their device shows digital RS due to the charge trapping/detrapping processes. However, the SET operation appeared to be forced by a wide voltage scan between −2.5 and 2.5 V, and the device essentially exhibited I−V curves similar to analog RS. The devices by Mishra et al. and Assi et al. showed high initial resistance values of ∼10^7 Ω, while the devices by Li et al. and Bala et al. exhibited lower OFF resistance values of 10^4−10^5 Ω in the pristine state. This difference in initial resistance may come from the deposition method as well as the thickness of the CuI films, which results in different stoichiometries and native defects. The measurement parameters, such as the voltage scan range, sweep rate, and current compliance value, were also different.

In this work, our Cu/CuI/Pt device showed a high initial resistance, despite the CuI film being relatively thin (60 nm). By carefully tuning the voltage sweep, the device first showed digital RS, but it transitioned to analog RS. After that, the device showed stable analog switching behavior. Therefore, we believe that the switching behavior of the CuI-based device is strongly dependent on the material/device parameters and measurement conditions. To determine the validity of the switching mechanism that we proposed, structural characterizations on the RS transition, such as X-ray photoemission spectroscopy and Fourier transform infrared spectroscopy, should be useful. However, since it is not possible to remove the upper electrode without damaging the CuI film, such analyses are difficult to apply at this stage. Further investigation is needed to clarify the correlation between the material, device, and measurement parameters and switching behavior.

4. CONCLUSIONS

In summary, we present the unique behavior of a Cu/CuI/Pt analog memristor device, based on a cross-point architecture. The device initially manifests distinct digital RS behavior under bias voltage sweeps, showing sharp SET and RESET processes with a high ON/OFF resistance ratio of ∼10^5. The digital RS is attributed to the formation and dissolution of Cu filaments based on the ECM mechanism. With increasing sweep cycles, the OFF resistance gradually decreased, and the SET/RESET processes became continuous. After 100 switching cycles, the device finally transitioned to analog RS behavior. This analog RS can be attributed to charge trapping/detrapping to acceptor vacancy sites, which were created during digital RS cycles. The device showing analog RS demonstrated various synaptic functionalities of long-term and short-term plasticity, including LTP, LTD, PPF, PPD, and STDP. Using the LTP and LTD characteristics, the ANN simulations exhibited an image recognition accuracy of ∼93% for handwritten digits from the MNIST data set. These findings indicate substantial potential of the CuI-based analog memristor to serve as an artificial synapse, thus offering promising avenues for applications in IMC and neuromorphic computing.

■ ASSOCIATED CONTENT

Supporting Information

The Supporting Information is available free of charge at https://pubs.acs.org/doi/10.1021/acsaelm.5c00529.

> Fabrication process of Cu/CuI/Pt devices, optical microscope images of CuI thin films spin-coated on SiO_2/Si substrates using different solvents, cross-sectional SEM of a CuI film spin-coated on a SiO_2/Si substrate, log−log plot of a typical I−V curve for a negative voltage sweep in analog RS mode, log−log plot of a typical I−V curve for a positive voltage sweep and Schottky barrier height variation plotted as a function of sweep cycles in digital RS mode, linear I−V curve showing the current-crossing point for digital and analog RS modes, energy band diagrams of a Cu/CuI/Pt structure before and after contact, retention property of a Cu/CuI/Pt device, nonlinearity coefficients of LTP/LTD data obtained from 20 voltage pulses, typical PPD behavior of a Cu/CuI/Pt device, and graphical representation of the input pulse scheme for STDP measurements (PDF)

■ AUTHOR INFORMATION

Corresponding Authors

Tohru Tsuruoka − *Research Center for Materials Nanoarchitectonics (MANA), National Institute for Materials Science (NIMS), Tsukuba 305-0044 Ibaraki, Japan;* orcid.org/0000-0002-4322-4309; Email: TSURUOKA.Tohru@nims.go.jp

Saumya R. Mohapatra − *Solid State Ionics Laboratory, Department of Physics, National Institute of Technology Silchar, Silchar 788010 Assam, India;* orcid.org/0000-0002-6753-5312; Email: saumya@phy.nits.ac.in

Authors

Rajesh Deb − *Solid State Ionics Laboratory, Department of Physics, National Institute of Technology Silchar, Silchar 788010 Assam, India*

Samapika Mallik − *Research Center for Materials Nanoarchitectonics (MANA), National Institute for Materials Science (NIMS), Tsukuba 305-0044 Ibaraki, Japan;* orcid.org/0000-0001-9281-9416

Yamineekanta Mishra − *Solid State Ionics Laboratory, Department of Physics, National Institute of Technology Silchar, Silchar 788010 Assam, India*

Roshan Padhan − *Laboratory for Low Dimensional Materials, Institute of Physics, Bhubaneswar 751005, India; Homi Bhabha National Institute, Mumbai 400094, India*

Satyaprakash Sahoo − *Laboratory for Low Dimensional Materials, Institute of Physics, Bhubaneswar 751005, India; Homi Bhabha National Institute, Mumbai 400094, India;* orcid.org/0000-0001-9766-3713

Kazuya Terabe − *Research Center for Materials Nanoarchitectonics (MANA), National Institute for Materials Science (NIMS), Tsukuba 305-0044 Ibaraki, Japan;* orcid.org/0000-0003-3988-3456

Complete contact information is available at: https://pubs.acs.org/10.1021/acsaelm.5c00529

Notes

The authors declare no competing financial interest.

■ ACKNOWLEDGMENTS

This work was supported in part by the Department of Science and Technology, Government of India, under the DST-FIST project (SR/FST/PSI-212/2016(C)), JSPS KAKENHI Grant Number 24K02917, and "Advanced Research Infrastructure for Materials and Nanotechnology in Japan (ARIM)" of the Ministry of Education, Culture, Sports, Science and Technology (MEXT). Proposal Number JPMXP1224NM5068.

■ REFERENCES

(1) Zhao, M.; Gao, B.; Tang, J.; Qian, H.; Wu, H. Reliability of analog resistive switching memory for neuromorphic computing. *Appl. Phys. Rev.* **2020**, *7*, No. 011301.

(2) Yin, Q. Y.; Yang, J.; Huang, K. Q.; Zhao, M. J.; Ni, W. C.; Liang, B.; Huang, Y.; Wu, S.; Wang, L. AI in human-computer gaming: Techniques, challenges and opportunities. *Mach. Intell. Res.* **2023**, *20*, 299−317.

(3) Seok, H.; Lee, D.; Son, S.; Choi, H.; Kim, G.; Kim, T. Beyond von Neumann architecture: Brain-inspired artificial neuromorphic devices and integrated computing. *Adv. Electron. Mater.* **2024**, *10*, No. 2300839.

(4) Tappertzhofen, S.; Mundelein, H.; Valov, I.; Waser, R. Nanoionic transport and electrochemical reactions in resistively switching silicon dioxide. *Nanoscale* **2012**, *4*, 3040−3043.

(5) Mannequin, C.; Tsuruoka, T.; Hasegawa, T.; Aono, M. Composition of thin Ta_2O_5 films deposited by different methods and the effect of humidity on their resistive switching behavior. *Jpn. J. Appl. Phys.* **2016**, *55*, No. 06GG08.

(6) Brivio, S.; Spiga, S.; Ielmini, D. HfO_2-based resistive switching memory devices for neuromorphic computing. *Neuromorphic Comput. Eng.* **2022**, *2*, No. 042001.

(7) Vishwanath, S. K.; Febriansyah, B.; Ng, S. E.; Das, T.; Acharya, J.; John, R. A.; Sharma, D.; Dananjaya, P. A.; Jagadeeswararao, M.; Tiwari, N.; Kulkarni, M. R. C.; Lew, W. S.; Chakraborty, S.; Basuf, A.; Mathews, N. High-performance one-dimensional halide perovskite crossbar memristors and synapses for neuromorphic computing. *Mater. Horiz.* **2024**, *11*, 2643−2656.

(8) Saleem, A.; Simanjuntak, F. M.; Chandrasekaran, S.; Rajasekaran, S.; Tseng, T. Y.; Prodromakis, T. Transformation of digital to analog switching in TaO_x-based memristor device for neuromorphic applications. *Appl. Phys. Lett.* **2021**, *118*, 112103.

(9) Zhu, Y.; Chen, M.; Lu, H.; Mi, P.; Luo, D.; Wang, Y.; Liu, Y.; Xiong, R.; Wang, H. The filaments control for tunning digital resistive switching in data storage application and analog behavior as an artificial synapse with $CsPbBr_3$-based memristor. *Appl. Phys. Lett.* **2024**, *124*, No. 063504.

(10) Guo, J.; Liu, L.; Bian, B.; Wang, J.; Zhao, X.; Zhang, Y.; Yan, Y. Ligand exchange reaction enables digital-to-analog resistive switching and artificial synapse within metal nanoparticles. *Adv. Funct. Mater.* **2023**, *33*, No. 2212666.

(11) Ngo, T. T.; Doan, U. T. T.; Vo, Q. T. T.; Huynh, T. L.; Vu, N. H.; Ta, H. K. T.; Hoa, L. T. M.; Kawazoe, Y.; Nguyen, P. T.; Pham, N. K. Study of digital and analog resistive switching memories based on methylammonium lead iodide ($MAPbI_3$) perovskite by experiments and DFT calculations. *J. Phys. D: Appl. Phys.* **2023**, *56*, 215301.

(12) John, R. A.; Yantara, N.; Ng, Y. F.; Narasimman, G.; Mosconi, E.; Meggiolaro, D.; Kulkarni, M. R.; Gopalakrishnan, P. K.; Nguyen, C. A.; Angelis, F. D.; Mhaisalkar, S. G.; Basu, A.; Mathews, N. Ionotronic halide perovskite drift-diffusive synapses for low-power neuromorphic computation. *Adv. Mater.* **2018**, *30*, No. 1805454.

(13) Greenlee, J. D.; Shank, J. C.; Tellekamp, M. B.; Doolittle, W. A. Spatiotemporal drift-diffusion simulations of analog ionic memristors. *J. Appl. Phys.* **2013**, *114*, No. 034504.

(14) Maas, K.; Villepreux, E.; Cooper, D.; Jimenez, C.; Roussel, H.; Rapenne, L.; Mescot, X.; Rafhay, Q.; Boudarda, M.; Burrie, M. Using a mixed ionic electronic conductor to build an analog memristive device with neuromorphic programming capabilities. *J. Mater. Chem. C* **2020**, *8*, 464−472.

(15) Singh, V. P.; Singh, C. P.; Ranjan, H.; Pandey, S. K. Investigation of analog resistive switching in solution-processed lead-free perovskite Cs_2SnI_6 memristor for synaptic application. *IEEE Trans. Electron Devices* **2023**, *70*, 5092−5098.

(16) Nayak, A.; Ohno, T.; Tsuruoka, T.; Terabe, K.; Hasegawa, T.; Gimzewski, J. K.; Aono, M. Controlling the synaptic plasticity of Cu_2S gap-type atomic switch. *Adv. Funct. Mater.* **2012**, *22*, 3606−3613.

(17) Zhu, X.; Li, D.; Liang, X.; Lu, W. D. Ionic modulation and ionic coupling effects in MoS_2 devices for neuromorphic computing. *Nat. Mater.* **2019**, *18*, 141−148.

(18) Shin, S.; Kang, D. C.; Kim, K.; Jeong, Y.; Kim, J.; Lee, S.; Kwak, J. Y.; Park, J.; Hwang, G. W.; Lee, K. S.; Park, J. K.; Li, J.; Kim, I. Emulating the short-term plasticity of a biological synapse with a ruthenium complex-based organic mixed ionic-electronic conductor. *Mater. Adv.* **2022**, *3*, 2827−2837.

(19) Yang, C.; Knei, M.; Schein, F. L.; Lorenz, M.; Grundmann, M. Room-temperature domainepitaxy of copper iodide thin films for transparent CuI/ZnO heterojunctions with high rectification ratios larger than 10^9. *Sci. Rep.* **2016**, *6*, No. 21937.

(20) Sharma, B.; Rabinal, M. K. Ambient Synthesis and Optoelectronic Properties of Copper Iodide Semiconductor Nanoparticles. *J. Alloys Compd.* **2013**, *556*, 198−202.

(21) Lee, S.; Lee, H. J.; Ji, Y.; Choi, S. M.; Lee, K. H.; Hong, K. Vacancy engineering of a solution processed CuI semiconductor: Tuning the electrical properties of inorganic p-channel thin-film transistors. *J. Mater. Chem. C* **2020**, *8*, 9608−9614.

(22) Mishra, D.; Mokurala, K.; Kumar, A.; Seo, S. G.; Jo, H. B.; Jin, S. H. Light-mediated multi-level flexible copper iodide resistive random access memory for forming-free, ultra-low power data storage application. *Adv. Funct. Mater.* **2023**, *33*, No. 2211022.

(23) Assi, D. S.; Huang, H.; Kandira, K. U.; Alsulaiman, N. S.; Theja, V. C. S.; Abbas, H.; Karthikeyan, V.; Roy, V. A. L. Charge-mediated copper-iodide-based artificial synaptic device with ultrahigh neuromorphic efficacy. *Phys. Status Solidi RRL* **2023**, *17*, No. 2300191.

(24) Li, B.; Wei, W.; Luo, L.; Gao, M.; Yu, Z. G.; Li, S.; Ang, K. W.; Zhu, C. Nonvolatile logic-in-memory computing based on solution-processed CuI memristor. *Adv. Electron. Mater.* **2022**, *8*, No. 2200089.

(25) Zhu, B. L.; Zhao, X. Z. Transparent conductive CuI thin films prepared by pulsed laser deposition. *Phys. Status Solidi A* **2011**, *208*, 91−96.

(26) Sirimanne, P. M.; Rusop, M.; Shirata, T.; Soga, T.; Jimbo, T. Characterization of CuI thin films prepared by different techniques. *Mater. Chem. Phys.* **2003**, *80*, 461−465.

(27) Zheng, Z.; Liu, A.; Wang, S.; Huang, B.; Wong, K. W.; Zhang, X.; Hark, S. K.; Lau, W. M. Growth of highly oriented (110) γ-CuI film with sharp exciton band. *J. Mater. Chem.* **2008**, *18*, 852−854.

(28) Markwitz, M.; Murmu, P. P.; Back, S. Y.; Mori, T.; Ruck, B. J.; Kennedy, J. Effect of grain boundary scattering on carrier mobility and thermoelectric properties of tellurium incorporated copper iodide thin films. *Surf. and Interfaces* **2023**, *41*, No. 103190.

(29) Yanga, C.; Kneiβ, M.; Lorenz, M.; Grundmann, M. Room-temperature synthesized copper iodide thin film as degenerate p-type transparent conductor with a boosted figure of merit. *Appl. Phys. Sci.* **2016**, *113*, 12929−12933.

(30) Balog, A.; Samu, G. F.; Kamat, P. V.; Janáky, C. Optoelectronic properties of CuI photoelectrodes. *J. Phys. Chem. Lett.* **2019**, *10*, 259−264.

(31) Gupta, R.; Modak, J. M.; Madras, G. Behavioral analysis of simultaneous photo-electro-catalytic degradation of antibiotic resistant E. coli and antibiotic via ZnO/CuI: a kinetic and mechanistic study. *Nanoscale Adv.* **2019**, *1*, 3992−4008.

(32) Deb, R.; Panda, D. M.; Nair, G.; Yasmin, F.; Mishra, Y.; Thakur, A. K.; Mohapatra, S. R. Diffusive memristor with CuS nanoparticles embedded in polymeric film as artificial nociceptor. *ACS Appl. Mater. Interfaces* **2024**, *16*, 51757−51768.

(33) Waser, R.; Dittmann, R.; Staikov, G.; Szot, K. Redox-based resistive switching memories - nanoionic mechanisms, prospects and challenges. *Adv. Mater.* **2009**, *21*, 2632−2663.

(34) Deb, R.; Nair, M. G.; Das, U.; Mohapatra, S. R. Contrasting analog and digital resistive switching memory characteristics in solution-processed copper (I) thiocyanate and its polymer electrolyte-based memristive devices. *J. Mater. Chem. C* **2023**, *11*, 7629−7640.

(35) Deb, R.; Pathak, P.; Mohapatra, S. R.; Das, U. Polarity independent resistive switching in MoS_2 nanosheets and PEO-based nanocomposite films. *Jpn. J. Appl. Phys.* **2022**, *61*, SM1004.

(36) Abbas, Y.; Jeon, Y. R.; Sokolov, A. S.; Kim, S.; Ku, B.; Choi, C. Compliance-free, digital SET and analog RESET synaptic characteristics of sub-tantalum oxide based neuromorphic device. *Sci. Rep.* **2018**, *8*, 1228.

(37) Luo, W.; Zeng, C.; Du, X.; Leng, C.; Yao, W.; Shi, H.; Wei, X.; Du, C.; Lu, S. Copper thiocyanate/copper iodide based hole transport composites with balanced properties for efficient polymer light-emitting diodes. *J. Mater. Chem. C* **2018**, *6*, 4895−4902.

(38) Valov, I.; Linn, E.; Tappertzhofen, S.; Schmelzer, S.; van den Hurk, J.; Lentz, F.; Waser, R. Nanobatteries in redox-based resistive switches require extension of memristor theory. *Nat. Commun.* **2013**, *4*, 1771.

(39) Grauzinye, M.; Botti, S.; Marques, M. A. L.; Goedecker, S.; Flores-Livas, J. A. Computational acceleration of prospective dopant discovery in cuprous iodide. *Phys. Chem. Chem. Phys.* **2019**, *21*, 18839.

(40) Wang, J.; Li, J.; Li, S. S. Native p-type transparent conductive CuI via intrinsic defects. *J. Appl. Phys.* **2011**, *110*, No. 054907.

(41) Ofuonye, B.; Lee, J.; Yan, M.; Sun, C.; Zuo, J. M.; Adesida, I. Electrical and microstructural properties of thermally annealed Ni/Au and Ni/Pt/Au Schottky contacts on AlGaN/GaN heterostructures. *Semicond. Sci. Technol.* **2014**, *29*, No. 095005.

(42) Wang, S.; Song, L.; Chen, W.; Wang, G.; Hao, E.; Li, C.; Hu, Y.; Pan, Y.; Nathan, A.; Hu, G.; Gao, S. Memristor-based intelligent human-like neural computing. *Adv. Electron. Mater.* **2023**, *9*, No. 2200877.

(43) Qin, L.; Cheng, S.; Xie, B.; Wei, X.; Jie, W. Co-existence of bipolar nonvolatile and volatile resistive switching based on WO_3 nanowire for applications in neuromorphic computing and selective memory. *Appl. Phys. Lett.* **2022**, *121*, No. 093502.

(44) Mallik, S. K.; Padhan, R.; Sahu, M. C.; Roy, S.; Pradhan, G. K.; Sahoo, P. K.; Dash, S. P.; Sahoo, S. Thermally driven multilevel non-volatile memory with monolayer MoS_2 for brain-inspired artificial learning. *ACS Appl. Mater. Interfaces* **2023**, *15*, 36527−36538.

(45) Mallik, S. K.; Padhan, R.; Sahu, M. C.; Pradhan, G. K.; Sahoo, P. K.; Dash, S. P.; Sahoo, S. Ionotronic WS_2 memtransistors for 6-bit storage and neuromorphic adaptation at high temperature. *npj 2D Mater. Appl.* **2023**, *7*, 63.

(46) Li, C.; Zhang, X.; Chen, P.; Zhou, K.; Yu, J.; Wu, G.; Xiang, D.; Jiang, H.; Wang, M.; Liu, Q. Short-term synaptic plasticity in emerging devices for neuromorphic computing. *iScience* **2023**, *26*, No. 106315.

(47) Mallik, S.; Tsuruoka, T.; Tsuchiya, T.; Terabe, K. Effects of Mg doping to a $LiCoO_2$ channel on the synaptic plasticity of Li ion-gated transistors. *ACS Appl. Mater. Interfaces* **2023**, *15*, 47184−47195.

(48) Yang, F. S.; Li, M.; Lee, M. P.; Ho, I. Y.; Chen, J. Y.; Ling, H.; Li, Y.; Chang, J. K.; Yang, S. H.; Chang, Y. M.; Lee, K. C.; Chou, Y. C.; Ho, C. H.; Li, W.; Lien, C. H.; Lin, Y. F. Oxidation-boosted charge trapping in ultrasensitive van der Waals materials for artificial synaptic features. *Nat. Commun.* **2020**, *11*, 2972.

(49) Jena, A. K.; Sahu, M. C.; Mohanan, K. U.; Mallik, S. K.; Sahoo, S.; Pradhan, G. K.; Sahoo, S. Bipolar resistive switching in TiO_2 artificial synapse mimicking Pavlov's associative learning. *ACS Appl. Mater. Interfaces* **2023**, *15*, 3574−3585.

(50) Tan, H.; Majumdar, S.; Qin, Q.; Lahtinen, J.; Dijken, S. V. Mimicking neurotransmitter release and long-term plasticity by oxygen vacancy migration in a tunnel junction memristor. *Adv. Intell. Syst.* **2019**, *1*, No. 1900036.

(51) Sahu, M. C.; Jena, A. K.; Mallik, A. K.; Roy, S.; Sahoo, S.; Ajimsha, R. S.; Misra, P.; Sahoo, S. Reconfigurable low-power TiO_2 memristor for integration of artificial synapse and nociceptor. *ACS Appl. Mater. Interfaces* **2023**, *15*, 25713−25725.

(52) Bala, A.; Pujar, P.; Daw, D.; Cho, Y.; Naqi, M.; Cho, H.; Gandla, S.; Kim, S. Transparent and flexible copper iodide resistive memories processed with a dissolution-recrystallization solution technique. *ACS Appl. Electron. Mater.* **2022**, *4*, 3973−3979.